Multi-physics Design of High-Energy-Density Wound Components

N. Simpson, R. Wrobel and P. H. Mellor
Department of Electrical and Electronic Engineering
University of Bristol
Bristol, UK
nick.simpson@bristol.ac.uk

***Abstract*—In this paper a computationally efficient high-fidelity multi-physics design tool applicable to E-core power inductors is developed. The tool is composed of 2-D electromagnetic and 3-D thermal finite analyses coupled to models for inductor core and winding loss. The models are fully parametrically defined and appear as a black-box problem which can be used to perform parameter studies or design optimisation. For example, the influence of strip or edge wound rectangular conductors on ac loss generation and thermal performance can be evaluated or inductor designs which satisfy a given specification can be identified. The tool is demonstrated by the design and experimental test of a high-energy-density filter inductor for an automotive application.**

I. Introduction

Wound passive components are a necessary part of a power electronic system, however, they contribute significantly to the overall volume, mass and losses of a power converter, [1]–[3], and are often the components limiting the overall mass or volume power density, [4]. Typically they represent around half the mass of a packaged power converter, in some cases their contribution is up to 70 %, [5]. In automotive and aerospace applications where mass and space are at a premium it is desirable to minimise the system mass and consequently maximise power density.

A reduction in wound component volume and mass can be achieved by increasing the operating frequency and by fully utilising the core and conductor materials to the limit of their magnetic flux density and current density respectively, [4]. However, under these operating conditions the core and winding losses become significant which has a detrimental effect on the efficiency of the component. Furthermore, the losses are temperature sensitive and tend to increase with temperature, therefore, adequate cooling is required to evacuate the loss and maintain an operating temperature below the thermal limit of the insulating materials. The design challenge is to identify an ideal balance between the internally generated loss, geometric dimensions and temperature rise of a wound component, resulting in an overall improvement in converter mass and volume, [5], [6]. This can only be accomplished through coupled electromagnetic, loss and thermal analyses.

An ideal multi-physics design tool would consist of high-fidelity electromagnetic and thermal models which iteratively exchange loss and temperature information to yield a detailed and accurate prediction of the electromagnetic and thermal behaviour. This analysis could then be used to perform parameter or sensitivity studies or be integrated into an optimisation routine to automatically guide the design parameters to meet a desired specification. However, the computational cost of high-fidelity models and the iterative nature of coupled problems and optimisation often prohibit their use, [7]–[9].

In this paper, a high-fidelity coupled electromagnetic and thermal design tool applicable to E-core power inductor design is developed. The modelling methods, tool structure and model coupling are selected to provide a favourable trade-off between the solution time, accuracy and detail. The models cater for non-transposed winding configurations, including circular and rectangular strip or edge wound variants, and are parametrically defined to enable parameter studies or design optimisation to be performed. The tool is demonstrated by the design and experimental test of a high-energy-density filter inductor for an automotive application.

II. Overview of the Design Tool

The design tool is composed of coupled electromagnetic and thermal analyses, formulated as a "black-box" problem, nested within an iterative optimisation procedure, as illustrated in Fig. 1. The optimisation procedure is used to steer the geometry and design parameters to identify candidate designs that satisfy a given specification. A 2-D electromagnetic Finite Element (FE) model is coupled to a steady-state 3-D thermal FE model through a core and ac winding loss model. The loss models take the form of analytical expressions which are informed by the electromagnetic analysis. The loss expressions are incorporated into the thermal model as local loss sources and are iteratively updated with temperature independently of the electromagnetic model. Hence, the electromagnetic and thermal models are loosely coupled, allowing the number of electromagnetic FE evaluations to be minimised, thereby, reducing the overall computation time. Parametric studies can be performed by evaluating the multi-physics analysis as a function of a parameter of interest independently of the optimisation procedure.

A. Electromagnetic Model

A parametric time-harmonic 2-D FE model is used to predict the electromagnetic behaviour and losses. The model accounts for non-linear saturation of the core material and

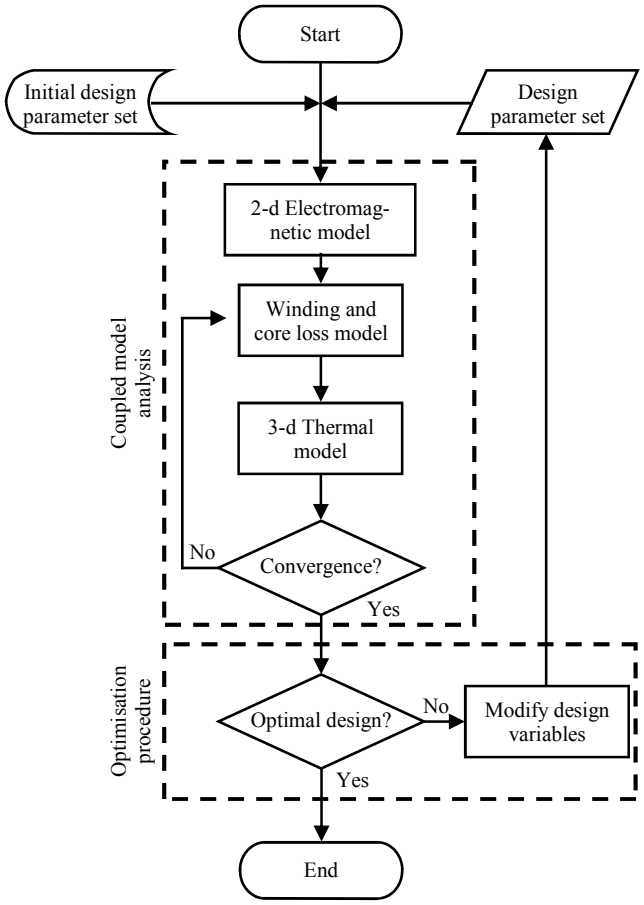

Fig. 1. An overview flow chart of the design tool structure.

enables winding eddy currents arising from ac proximity and skin effects to be identified, as illustrated in Fig. 2. Due to symmetry, only one half of the inductor cross-section is modelled. The transposition of conductors such as that found in Litz wire and proximity losses induced in the casing are not directly catered for although these could be incorporated with an appropriate model adjustment. Pure sinusoidal excitation current is assumed, however, non-sinusoidal current can be approximated by decomposing the waveform into its Fourier components and evaluating the model at each significant harmonic along with the dc average and superimposing the result, [4]. The contribution of the end-windings to the inductance and ac loss is assumed to be negligible and is confirmed using a 3-D FE model as a post-design validation step.

A set of FE analyses with varying winding current levels, operating frequencies and conductor conductivities (emulating a varying operating temperature) are required to characterise the inductor. These analyses are independent of one another and are evaluated in parallel in order to take advantage of modern multi-core desktop computing hardware and minimise the solution time of the electromagnetic modelling stage.

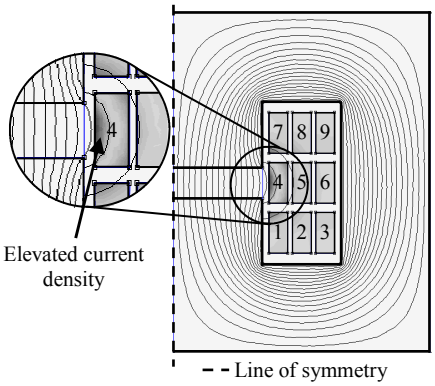

Fig. 2. Example of the 2-D electromagnetic FE model operating at 200 A_{rms} and 400 Hz.

B. Winding and Core Loss Models

1) Winding Loss: The single turn winding loss is composed of a dc component and an ac component arising from proximity and skin effects, each of which are temperature dependent, [10]. The ac effects result in a non-uniform current density distribution across the winding, as illustrated in Fig. 2. A common figure of merit used to describe the ac loss effect is the ratio of the equivalent ac to dc resistance, R_{ac}/R_{dc}. This ratio can be estimated by evaluating the electromagnetic FE model for each frequency and temperature of interest, however, this approach is computationally intensive and can lead to prohibitive solution times. An alternative technique is employed here, which requires a minimum set of FE analyses to inform a loss function which scales the ac loss with temperature, [11].

$$R_{dc} = \frac{\rho \bar{l}}{A}\left(1 + \alpha\left(T_{op} - T_0\right)\right) \tag{1}$$

The well established expression for dc winding resistance, R_{dc}, is presented in (1) which is assumed to vary as a linearised function of temperature, where ρ, $\bar{l}$, A, α, T_{op}, T_0 are the electrical conductivity, mean path length, cross-sectional area, temperature coefficient of resistance, operating temperature and reference temperature respectively.

$$\left.\frac{R_{ac}}{R_{dc}}\right|_{T_{op}} = \frac{\left(\left.\frac{R_{ac}}{R_{dc}}\right|_{T_0} - 1\right)}{\left(1 + \alpha\left(T_{op} - T_0\right)\right)^{\beta+1}} + 1 \tag{2}$$

$$\beta = \frac{\log\left(\left.\frac{R_{ac}}{R_{dc}}\right|_{T_0} - 1\right) - \log\left(\left.\frac{R_{ac}}{R_{dc}}\right|_{T_{max}} - 1\right)}{\log\left(1 + \alpha\left(T_{max} - T_0\right)\right)} - 1 \tag{3}$$

The simplicity inherent in (1) can be extended to ac loss effects. An approximation of R_{ac}/R_{dc} at the operating temperature, T_{op}, is given by (2), [11], where , $R_{ac}/R_{dc}|_{T0}$, α and β are the R_{ac}/R_{dc} ratio evaluated using the FE model at the reference temperature, T_0, the temperature coefficient of resis-

tance and a curve fitting term respectively. The exponent, β, is frequency dependent and is found from (3) using the R_{ac}/R_{dc} value evaluated at the reference temperature, T_0, and a further R_{ac}/R_{dc} value evaluated at the maximum expected operating temperature, T_{max}. The reference and maximum operating temperature are simulated in the FE model by linearly scaling the electrical conductivity of the winding material using the coefficient of resistance, α, as in (1). Hence, the ac loss of the winding is approximated as a function of temperature at a single frequency using only two electromagnetic FE analyses which leads to a significant reduction in computation time.

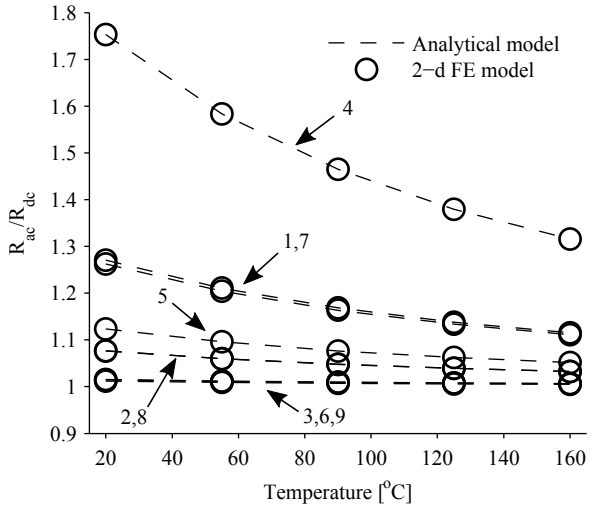

Fig. 3. Comparison of R_{ac}/R_{dc} predicted using 2-D FE analysis and (2).

Fig. 3 shows a close agreement between the R_{ac}/R_{dc} values predicted using (2) and those calculated using the electromagnetic FE model for each of the nine conductors of the winding illustrated in Fig. 2. It is evident that the conductors in close proximity to the air-gap fringing field $(Nos.\ 1, 4, 7)$ can exhibit a significantly higher ac loss than those furthest away from the air-gap $(Nos.\ 3, 6, 9)$. The R_{ac}/R_{dc} ratio decreases with increasing temperature as a result of the increased conductor resistivity which acts to reduce the flow of eddy currents. The non-uniform loss distribution across the winding can impact the location and magnitude of the winding hot-spot, hence a unique loss expression is derived for each conductor. Only dc loss scaled with temperature, (1), is accounted for in end-winding, the ac loss contribution is assumed to be negligible.

2) Core Loss:

$$W_{Fe} = k_h f B^{\alpha_{fe}} + k_e f^2 B^2 + k_a f^{1.5} B^{1.5} \qquad (4)$$

The losses manifesting within the core resulting from hysteresis, eddy currents and excess loss are estimated using the Bertotti iron loss model, (4), [12], where f and B are the frequency and peak flux density respectively. The coefficients, $k_h = 1.11 \times 10^{-2}$, $\alpha_{fe} = 2.95$, $k_e = 1.55 \times 10^{-5}$ and $k_a = 6.44 \times 10^{-4}$ are determined by minimising the error between (4) and measured data provided by the electrical steel manufacturer. The flux density distribution in the core is obtained from the electromagnetic FE model and used to estimate the average core loss which is applied globally to the core region in the thermal model.

C. Thermal Model

A parametric steady-state 3-D FE model is used to predict the thermal behaviour of the inductor, Fig. 4. It is assumed that the inductor is potted and housed within a case that is mounted to a cold plate at a fixed temperature, hence, the model is reduced to a pure conduction problem with boundary conditions. The cold plate is emulated by a fixed temperature boundary condition applied to the bottom of the inductor case. Adiabatic boundary conditions are assumed on the remaining surfaces since the heat extraction by the cold plate dominates over natural convection and radiation mechanisms. The model caters for windings formed from either rectangular or round non-transposed conductors arranged in a regular pattern. Due to symmetry only one quarter of the inductor is modelled.

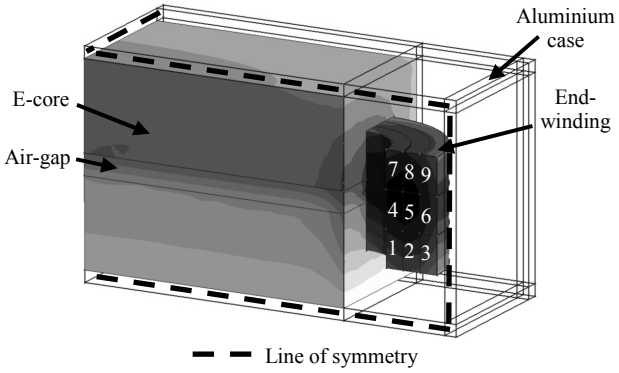

Fig. 4. Example of the 3-D thermal FE model.

The slot liner used to provide electrical and mechanical protection to the winding is represented in the thermal model as it acts as a thermal barrier, impeding the flow of heat from the winding to the core and has a significant impact on the winding temperature, [13]. The impregnated winding is a composite material composed of conductor, electrical insulation and encapsulant insulation materials. Representing the geometry of each conductor, insulation layer and the surrounding encapsulant would add significant complexity to the thermal model and increase solution times, particularly for high conductor numbers, due to the increased number of unknowns to solve and the added difficulty in the model meshing. Therefore, following common practise, the winding is represented as a homogeneous anisotropic lumped region with equivalent thermal properties, [13], [14]. The equivalent thermal conductivity and specific heat capacity of the winding are estimated using a numerical FE model of a heat-flow meter and an analytical expression based on the relative volume of the constituent materials, respectively. The estimation methods are experimentally validated using measurements performed on a range of impregnated winding samples with varying fill factors and conductor profiles, [15].

The lumped winding region is divided into regular sub-regions with equal cross-section representing the individual

conductors within the winding, Fig. 4. Unique loss expressions informed from the electromagnetic model, Sections II-A and II-B, are applied to each active length and end-winding region as a local loss source in order to account for the non-uniform temperature sensitive loss distribution and give an accurate estimate of the winding hot-spot temperature and location.

D. Optimisation Routine

The multi-physics analysis is formulated as a "black-box" problem to enable parameter studies or design optimisation to be performed using any suitable parameter sweeping algorithm or optimisation routine. In the present implementation, Particle Swarm Optimisation (PSO) is employed to systematically vary the design parameters within predetermined bounds and identify inductor designs which satisfy a desired specification, as illustrated in Fig. 1, [16], [17].

III. Filter Inductor Design Case Study

The multi-physics tool is demonstrated by the design of an $80\ \mu H$, $200\ A_{rms}$ filter inductor intended to be integrated into the power electronic stage and water cooling circuit of an automotive power converter. The cooling circuit is assumed to be at an ambient temperature of $80\ ^oC$. The full inductor specification is given in Table I.

TABLE I
Inductor specification

Parameter	Value	Unit
Current rating, I_{rms}	200	A
Operating frequency, f_{op}	400	Hz
Inductance, L_t	80	μH
Maximum operating temperature, T_t	180	^oC
Target energy density (complete assembly), E_{dt}	1.2	J/kg

$$E_d = \frac{LI_{pk}{}^2}{4M} = \frac{LI_{rms}{}^2}{M} \tag{5}$$

The main design driver is the mass energy density, E_d, (5), which is defined as the energy stored in the magnetic field per unit mass of the complete inductor assembly including the case. Where L, M, I_{pk} and I_{rms} are the inductance, mass and peak and rms winding current respectively. A secondary design driver is the manufacturing cost. Aluminium conductors are selected over copper due to their lower cost and potential to save mass in the design. A single layer strip winding is assumed to simplify the manufacture.

A. Objective Function Definition

The objective function, $E(D_p)$, (6), quantitatively represents the extent to which a candidate design, described by the design parameter set D_p, Table II, satisfies the specification, Table I. $E(D_p)$ is formulated as a sum of three normalised error terms representing the deviation of a candidate design from the inductance, L_t, energy density, E_{dt}, and peak operating temperature, T_t, targets. The objective function returns zero for a design that completely satisfies the specification.

$$E(D_p) = \left|\frac{L_t - L_c(D_p)}{L_t}\right| + \left|\frac{E_{dt} - E_{dc}(D_p)}{E_{dt}}\right| + \left|\frac{T_t - T_c(D_p)}{T_t}\right| \tag{6}$$

TABLE II
Inductor design parameters

Parameter	Value Range	Unit
Core thickness*, T_{core}	$1 \leq T_{core} \leq 50$	mm
Number of turns, N_t	$1 \leq N_t \leq 75$	n/a
Air-gap length (normalised), L_{ag}	$0.01 \leq L_{ag} \leq 0.99$	n/a
Active length*, L_{act}	$1 \leq L_{act} \leq 300$	mm
Conductor current density, J_c	$1 \leq J_c \leq 40$	A/mm^2
Aspect ratio*, AR	$0.1 \leq AR \leq 10$	n/a

* refer to Figs. 2 and 4

B. Optimised Inductor Design

The PSO procedure seeks to minimise $E(D_p)$, (6), by iteratively searching for an appropriate design parameter set, D_p, in the range of Table II. The objective function is multi-valued meaning that a number of design parameter sets, D_p, can equally satisfy the design specification. In this study, the design tool is used to generate a set of 150 design candidates and identify a Pareto optimal set, [18]. An example of the objective function value, (6), as a function of each PSO generation for three of the candidate designs is shown in Fig. 5.

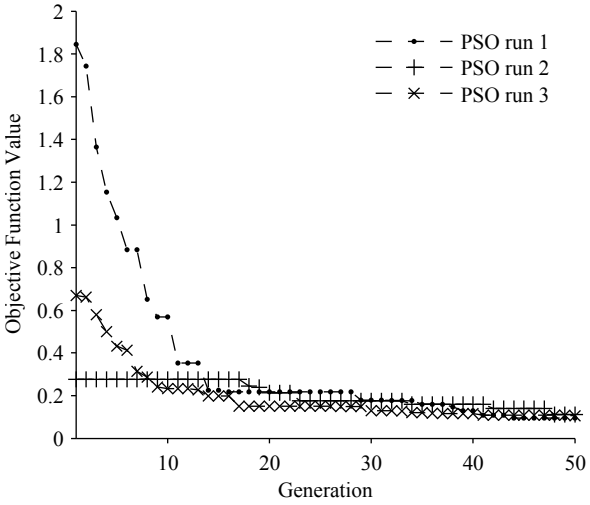

Fig. 5. Objective function value of three candidate designs.

Each candidate design shows similar characteristics with the primary difference being the active length, L_{act}, aspect ratio, AR, mass and generated loss. The Pareto optimal set is used to select a design that not only meets the specification but provides the most beneficial trade-off between loss and mass, [18]. The average objective function value of the selected design was 8.6×10^{-2} after 50 generations taking approximately 11 and $1/4$ hours to complete. The resulting inductor design is within 5% ($76\ \mu H$), 1.7% ($177\ ^oC$) and

1.7% (1.18) of the inductance, temperature and energy density targets respectively.

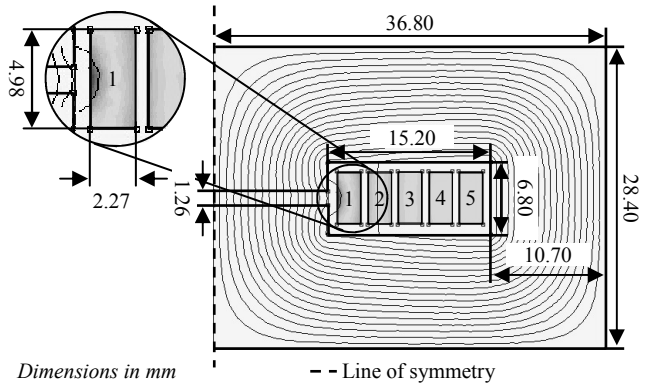

Fig. 6. Inductor cross-section showing flux lines and conductor current density, 200 A_{rms}, 400 Hz.

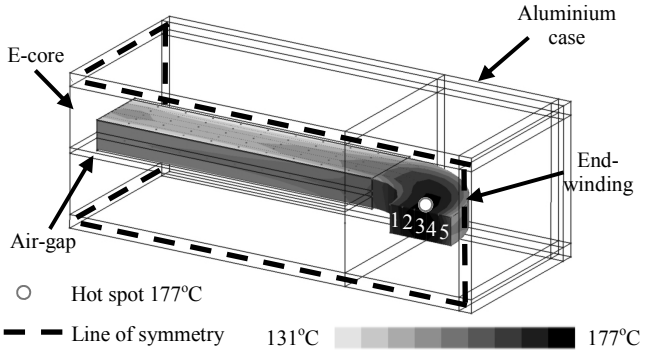

Fig. 7. 3-D thermal FE model, 200 A_{rms}, 400 Hz

TABLE III
OPTIMISED INDUCTOR DESIGN PARAMETERS

Parameter	Value	Unit
Core thickness, T_{core}	10.7	mm
Number of turns, N_t	5	n/a
Air-gap length, L_{ag}	1.26	mm
Active length, L_{act}	133.6	mm
Conductor current density, J_c	17.6	A/mm^2
Aspect ratio, AR	2.24	n/a

The inductor cross-section and design parameters are given in Fig. 6 and Table III respectively. The inductor winding is composed of 5 turns of 5×3 mm rectangular profile aluminium wire operating at an rms current density of 17.6 A/mm^2. The steady state winding and core loss at 400 Hz and 200 A_{rms} are estimated to be 312 W and 62 W respectively resulting in a winding hot-spot temperature of 177 ^oC, as illustrated in Fig. 7.

C. 3-d FE Validation of the Electromagnetic Model

The 2-D electromagnetic FE model does not account for the contribution of the end-winding to the inductance and ac loss, Section II-A. The filter inductor design has a large active length to end-winding length ratio, hence, the end-winding is predicted to account for only 26 % of the total winding loss. Consequently the end-winding ac loss is expected to be negligible with respect to the total winding loss. In order to validate this hypothesis the inductor performance is predicted using a time-harmonic 3-D electromagnetic FE model and the results compared to the 2-D model predictions.

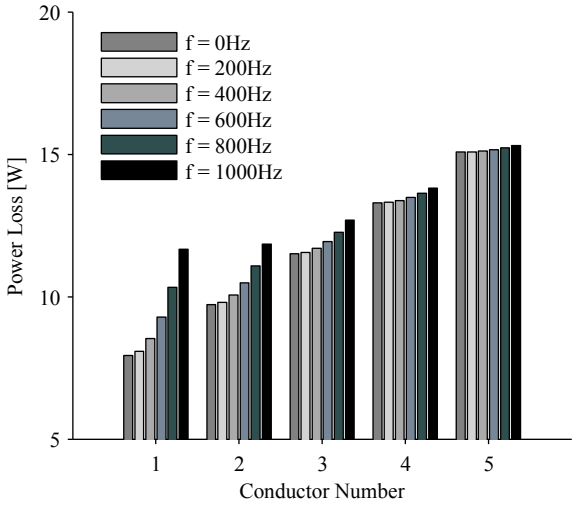

Fig. 8. End-winding loss at 200 A_{rms} and 20 ^oC.

The dc winding resistance predicted by the 2-D and 3-D models differ by less than 1 % between 20 ^oC and 200^oC. Fig. 8 shows the end-winding ac loss for each of the 5 winding turns predicted using the 3-D FE model at a winding current of 200 A_{rms} in the frequency range $0-1$ kHz at 20 ^oC. The length of the end-turn increases from conductor 1 to 5, hence the dc loss of each conductor increases proportionally. The ac loss increases as a function of frequency with the highest proportional loss increase experienced by the innermost conductor $(No.\ 1)$ which is more exposed to the time-varying air-gap fringing field, Fig. 6. At the intended operating frequency of 400 Hz there is an average increase in loss over the dc value by 0.7 % at 20 ^oC and 0.2 % at 200 ^oC. However, the absolute contribution of the end-winding ac loss to the total winding loss is less than 2 % over the 20 ^oC to 200 ^oC temperature range. The total ac winding loss predicted by the 2-D model is within 2.5 % at 20 ^oC and within 0.9 % at 200 ^oC of the 3-D model prediction. The core loss predictions of the 2-D and 3-D models at 400 Hz and 200 A_{rms} are within 5 % at 62 W and 59 W respectively.

Fig. 9 shows the inductance as a function of rms current predicted by the 2-D and 3-D models. The 3-D model prediction is an average of 3 % higher than the 2-D model over the current range $5-200$ A_{rms}. The maximum deviation of 7 % occurs at the rated 200 A_{rms}. The inductance begins to reduce from approximately 150 A_{rms} in both models due to the onset of core saturation, however, the gradient is lower in the 3-D model prediction. This is attributed to the additional flux linking the end-winding contributing to the inductance which is not accounted for in the 2-D model.

The 3-D model inductance prediction is 7 % higher than the 2-D prediction at rated current which better satisfies the specification in this case, Table I. The 2-D and 3-D model predictions of core and ac loss show close agreement in the

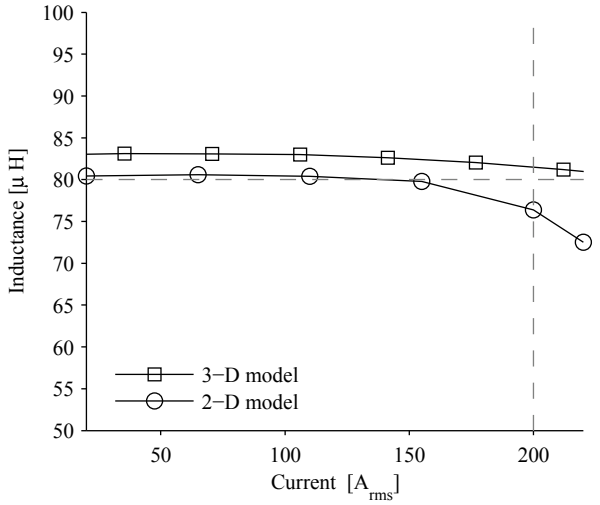

Fig. 9. Inductance as a function of excitation current.

case of the filter inductor design, hence the assumption of dc loss in the end-winding region is valid. However, this assumption cannot be generalised since the end-winding ac loss is strongly dependent on the conductor arrangement and the proximity to the air-gap fringing field which differ for varying core geometry and winding configurations. Therefore, the end-winding ac loss can become significant with respect to the total winding loss for some designs, particularly those with a low active-length to end-winding length ratio, and should ideally be accounted for in the design tool models, [10], [19].

IV. Inductor Construction

In order to assess the validity of the design tool models, the filter inductor is manufactured and subjected to experimental tests. The inductor core is composed of E-core sections cut from a pre-bonded stack of NO20 $0.2\ mm$ electrical steel laminations using an Electrical Discharge Machining (EDM) process, Fig. 10. The winding is constructed using $5 \times 2.3\ mm$ nominal sized polyamide-imide insulated aluminium conductors rated to $200\ ^oC$. The prototype aluminium winding is transitioned to a copper terminal using bi-metallic lug crimps, however, in volume production cold or ultrasonic welding would become economically viable and reduce the termination size.

A slot liner is used to protect the coil from abrasion and improve the electrical insulation, however, the low thermal conductivity of the material $(0.1\ W/m.K)$ tends to impede heat flow. The slot liner is precision laser cut to ensure good contact between the winding, slot liner and core to maximise heat transfer, [13]. Fibreglass sleeving is used to protect the winding insulation during termination. PEEK inserts electrically isolate the exposed aluminium crimps from the casing. Type k thermocouples are placed and adhered as shown in Fig. 10. The inductor is potted using a high thermal conductive potting compound $(1.27\ W/m.K)$, Silcotherm SE2003. The potting compound has a high mixed viscosity $(35\ Pas)$ due to the inclusion of a filler and is not compatible with the vacuum

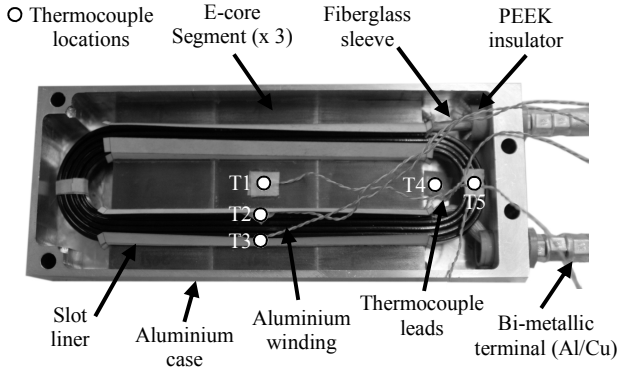

Fig. 10. Partially constructed filter inductor.

impregnation equipment available at the time of manufacture. Therefore, the potting compound is manually painted onto the winding and into the air-gap and end-space regions, ensuring a thorough infiltration of cavities. The case is sealed and clamped in place during the inductor cure cycle at $100\ ^oC$ for 4 hours. The prototype inductor and associated cold-plate are shown in Fig. 11.

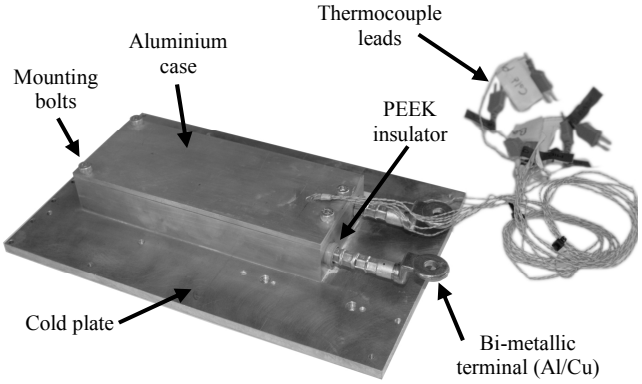

Fig. 11. Complete prototype filter inductor and associated cold plate.

V. Experimental Test

A. Steady-state dc Thermal Measurement

The experimental set up used for steady-state dc thermal tests is shown in Fig. 12. The inductor is insulated using Zotek N high temperature foam to approximate adiabatic conditions. The inductor is affixed to a cold plate which is controlled to a temperature of $80\ ^oC$ using an ATC K3 cooling unit. An EA-PS 8080-510 dc power supply provides winding current, measured using an LEM 400-S high precision current transducer. An Agilent 34972A data logger records the thermocouple temperatures, Fig. 10, winding voltage drop and current.

The steady-state temperature distribution and power are measured at winding current levels up to $200\ A_{rms}$ in $50\ A$ increments. Fig. 13 shows the temperatures predicted by the design tool, accounting for dc loss only, Section II-C, and measured in the steady-state at $200\ A_{rms}$. The 3-D FE model consistently under predicts the temperature distribution of the

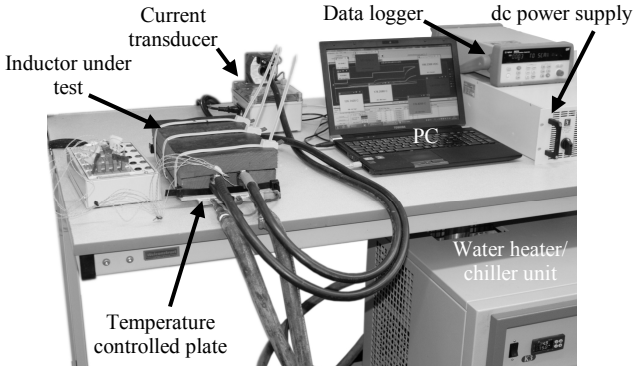

Fig. 12. Experimental set up for dc steady-state thermal tests.

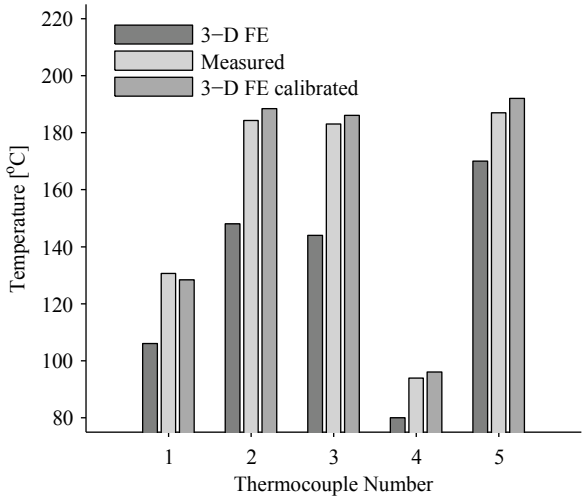

Fig. 13. 3-D FE, measured and calibrated 3-D FE temperature measurements.

inductor by an average of 26 ^oC with a worst case of 39 ^oC for the prediction of the active length winding temperature (thermocouple 3), Fig. 10.

A 6 % discrepancy between the predicted $(4.8\ m\Omega)$ and measured $(5.1\ m\Omega)$ dc winding resistance is observed at 20 ^oC, not including the crimped terminations leading to an under prediction of the dc winding loss. This is attributed to the difference between the desired and practical conductor dimensions along with the rounded edges of the conductor profile and additional conductor length required to terminate the winding. The design tool is updated to reflect these quantifiable differences.

The inductor is mounted on a 6 mm thick aluminium plate, Fig. 11, which is in turn mounted to a temperature controlled cold plate at 80 ^oC . The thermal interface resistance between the cold plate and the inductor base (thermocouple 4) results in a 13 ^oC temperature difference which is reflected in the thermal model by increasing the case boundary condition temperature to 93 ^oC, Fig. 4. A 1 mm gap is introduced between the case and the inductor core to emulate the thermal interface which has a significant effect on the heat extraction from the core, [13]. The equivalent thermal conductivity of the gap is set to 20 $W/m.K$ which approximates steel in contact with aluminium at a moderate pressure, [20]. The potting of the inductor was performed manually to ensure a high quality infiltration, however, a small amount of material was lost during the curing cycle due to thermal expansion. The thermal conductivity of the potting material was reduced by 10 % to emulate the imperfect impregnation. The predicted temperature distribution was calibrated against the measured data by reducing the slot liner thermal conductivity by 39 % to account for the imperfect thermal contact at the slot liner, core and winding interfaces. The temperature predictions of the updated and calibrated thermal model are illustrated in Fig. 13. The steady state loss prediction is within 4 % of the measured value and the temperatures are overestimated by approximately 3 %. The close agreement between the predicted and measured temperature distribution after a simple calibration indicates that the thermal model is well formulated. The interface gaps between components have a significant impact on performance and are difficult to predict at the design stage, [13], [20], [21]. In order to improve future temperature predictions, the thermal model is updated to include the component interface gaps and calibration, which reflect typical manufacturing processes. The calibration in the present study is based on tests performed on a single inductor, however, the prototype is part of a three-phase set, hence there is opportunity for further experimentation and comparative tests to establish a more representative set of calibration data.

B. Inductance Measurement

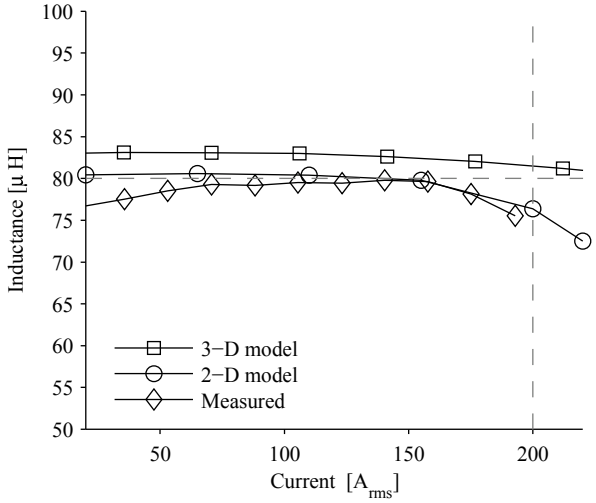

Fig. 14. Inductance as a function of excitation current.

The inductance of the filter inductor is measured as a function of excitation current using a large signal testing method which measures the change in flux linkage after a dc current is removed, [22]. The measurements and theoretical predictions presented in Fig. 14 show a good correlation. The average measured inductance of 78 μH is 5 % lower than the 3-D FE model estimate. The measured inductance at 275 A_{peak} is 7 % lower than that predicted by the 3-D model. This is commensurate with a 0.1 mm parasitic air-gap that is

attributed to a combination of manufacturing tolerances, core alignment and contamination of the E-core contacting surfaces during the potting process.

VI. Conclusion

In this paper a high-fidelity multi-physics design tool applicable to E-core power inductors is presented. The tool combines 2-D and 3-D electromagnetic and thermal FE models with an ac loss scaling technique to enable a minimal set of FE analyses to characterise the inductor performance, [11]. The tool caters for windings formed from regularly distributed non-transposed round or rectangular conductors in a strip or edge-wound configuration. Equivalent thermal properties of the winding amalgam are used to simplify the thermal model definition and reduce computation time, [15]. Non-uniform distribution of winding loss exhibited under ac operation is accounted for. The tool is demonstrated by the design of a high-energy-density filter inductor. The achieved specific energy of $1.2\ J/kg$ is representative of a factor of three mass saving compared to commercially available components. The 2-D electromagnetic and ac loss predictions show close agreement with a 3-D FE model used in post-design validation. The contribution of the end-winding region to ac loss and inductance is dependent on the relative active-winding and end-winding volume, conductor placement, air-gap and core geometry. In order to ensure the generality of the design tool, methods of accounting for these effects should be investigated, [10], [19].

Experimental tests performed on a prototype inductor show close agreement with the inductance and temperature estimates after model calibration and serve to highlight the necessity of including build factors such as thermal interface gaps in the thermal model definition, [13], [21]. Further tests on a three-phase set of inductors will better inform the thermal model definition and experimentally validate the core and ac loss predictions. The design tool provides a computationally efficient high-fidelity prediction of inductor behaviour and can be used to perform both parameter studies and design optimisation in order to allow a greater exploitation of materials and yield more compact and lighter designs, thereby improving the overall power density of a converter.

References

[1] T. Salem, D. Urciuoli, V. Lubomirsky, and G. Ovrebo, "Design considerations for high power inductors in dc-dc converters," in *Applied Power Electronics Conference, APEC 2007 - Twenty Second Annual IEEE*, Feb 2007, pp. 1258–1263.

[2] R. Wrobel, N. McNeill, and P. Mellor, "Performance analysis and thermal modeling of a high-energy-density prebiased inductor," *Industrial Electronics, IEEE Transactions on*, vol. 57, no. 1, pp. 201–208, Jan 2010.

[3] B.-G. You, B.-K. Lee, S.-W. Lee, M.-C. Jeong, J. hyung Kim, and I.-B. Jeong, "Improvement of the thermal flow with potting structured inductor for high power density in 40kw dc-dc converter," in *Vehicle Power and Propulsion Conference (VPPC), 2012 IEEE*, Oct 2012, pp. 1027–1032.

[4] M. Gerber, J. Ferreira, I. Hofsajer, and N. Seliger, "A high-density heatsink-mounted inductor for automotive applications," *Industry Applications, IEEE Transactions on*, vol. 40, no. 4, pp. 1031–1038, July 2004.

[5] G. Shane and S. Sudhoff, "Design paradigm for permanent-magnet-inductor-based power converters," *Energy Conversion, IEEE Transactions on*, vol. 28, no. 4, pp. 880–893, Dec 2013.

[6] K. Nakamura, H. Yoshida, and O. Ichinokura, "Electromagnetic and thermal coupled analysis of ferrite orthogonal-core based on three-dimensional reluctance and thermal-resistance network model," *Magnetics, IEEE Transactions on*, vol. 40, no. 4, pp. 2050–2052, July 2004.

[7] W. Jiang and T. Jahns, "Development of efficient electromagnetic-thermal coupled model of electric machines based on finite element analysis," in *Electric Machines Drives Conference (IEMDC), 2013 IEEE International*, 2013, pp. 816–823.

[8] I. Vese, F. Marignetti, and M. Radulescu, "Multiphysics approach to numerical modeling of a permanent-magnet tubular linear motor," *Industrial Electronics, IEEE Transactions on*, vol. 57, no. 1, pp. 320–326, 2010.

[9] N. Simpson, R. Wrobel, and P. Mellor, "A multi-physics design methodology applied to a high-force-density short-duty linear actuator," in *Energy Conversion Congress and Exposition (ECCE), 2014 IEEE*, Sept 2014, pp. 5168–5175.

[10] C. Sullivan, "Computationally efficient winding loss calculation with multiple windings, arbitrary waveforms, and two-dimensional or three-dimensional field geometry," *Power Electronics, IEEE Transactions on*, vol. 16, no. 1, pp. 142–150, Jan 2001.

[11] R. Wrobel, D. Salt, A. Griffo, N. Simpson, and P. Mellor, "Derivation and scaling of ac copper loss in thermal modeling of electrical machines," *Industrial Electronics, IEEE Transactions on*, vol. 61, no. 8, pp. 4412–4420, Aug 2014.

[12] M. Popescu, D. Ionel, A. Boglietti, A. Cavagnino, C. Cossar, and M. McGilp, "A general model for estimating the laminated steel losses under pwm voltage supply," *Industry Applications, IEEE Transactions on*, vol. 46, no. 4, pp. 1389–1396, July 2010.

[13] A. Boglietti, A. Cavagnino, and D. Staton, "Determination of critical parameters in electrical machine thermal models," *Industry Applications, IEEE Transactions on*, vol. 44, no. 4, pp. 1150–1159, 2008.

[14] L. Siesing, A. Reinap, and M. Andersson, "Thermal properties on high fill factor electrical windings: Infiltrated vs non infiltrated," in *Electrical Machines (ICEM), 2014 International Conference on*, Sept 2014, pp. 2218–2223.

[15] N. Simpson, R. Wrobel, and P. Mellor, "Estimation of equivalent thermal parameters of impregnated electrical windings," *Industry Applications, IEEE Transactions on*, vol. 49, no. 6, pp. 2505–2515, Nov 2013.

[16] N. Bracikowski, M. Hecquet, P. Brochet, and S. Shirinskii, "Multiphysics modeling of a permanent magnet synchronous machine by using lumped models," *Industrial Electronics, IEEE Transactions on*, vol. 59, no. 6, pp. 2426–2437, 2012.

[17] A. Sarikhani and O. Mohammed, "A multi-physics multi-objective optimal design approach of pm synchronous machines," in *Electrical Machines (ICEM), 2014 International Conference on*, Sept 2014, pp. 968–974.

[18] N. Simpson and P. Mellor, "Exploiting cloud computing in the multi-physics design and optimisation of electromagnetic devices," in *Control and Modeling for Power Electronics (COMPEL), 2015 IEEE 16th Workshop on*, [In Press].

[19] J. Potgieter and M. Kamper, "Calculation methods and effects of end-winding inductance and permanent-magnet end flux on performance prediction of nonoverlap winding permanent-magnet machines," *Industry Applications, IEEE Transactions on*, vol. 50, no. 4, pp. 2458–2466, July 2014.

[20] Y. A. Cengel, *Heat and Mass Transfer: a practical approach*. Tata McGraw-Hill Education, 2007.

[21] D. Staton, A. Boglietti, and A. Cavagnino, "Solving the more difficult aspects of electric motor thermal analysis in small and medium size industrial induction motors," *Energy Conversion, IEEE Transactions on*, vol. 20, no. 3, pp. 620–628, Sept 2005.

[22] S. Yamamoto, T. Ara, S. Oda, and K. Matsuse, "Prediction of starting performance of pm motors by dc decay testing method," *Industry Applications, IEEE Transactions on*, vol. 36, no. 4, pp. 1053–1060, Jul 2000.